LASERS AND AMPLIFIERS

PACS numbers: 42.55.Lt; 42.60.Jf; 42.60.Lh
DOI: 10.1070/QE2008v038n04ABEH013697

Kinetics of the active medium of a He–Sr^+ recombination laser: 1. Spatiotemporal characteristics

G.D. Chebotarev, E.L. Latush, O.O. Prutsakov, A.A. Fesenko

Abstract. **A self-consistent mathematical model of a $He-Sr^+$ recombination laser is developed and used to study the establishment of a repetitively pulsed regime in the active medium. The spatiotemporal characteristics are analysed in the stationary regime under different excitation conditions, the contraction of a repetitively pulsed discharge in helium is investigated and the discharge decontraction upon addition of strontium vapour, which is fundamentally important for metal vapour lasers is studied. Numerical simulations are shown to be a convenient tool for investigating the kinetics of the active medium of a $He-Sr^+$ laser, which enables predicting the optimal excitation conditions and calculating the limiting lasing characteristics.**

Keywords: *$He-Sr^+$ recombination laser, repetitively pulsed regime, spatiotemporal characteristics, mathematical simulation.*

1. Introduction

$He-Sr^+$ lasers belong to the category of ion recombination metal vapour lasers [1 – 4]. The lasing wavelength range (the 430.5- and 416.2-nm lines of Sr II ions) and the high output power (up to several watts) make them attractive for practical applications.

The active medium of this laser is a mixture of strontium vapour and helium. The required vapour density is achieved by heating the active region, which is commonly performed in the self-heating regime. The active medium is excited by short current pulses (~ 0.1 μs), during which an almost total two-fold ionisation of strontium occurs. The plasma recombines after completion of the current pulse. The $6S_{1/2}$ upper laser level (Fig. 1) is pumped in the collisional-radiative recombination $Sr^{++} + 2e \rightarrow Sr^{+*} + e$ during the early afterglow, while the population inversion is achieved due to the efficient depopulation of the $5P_{1/2}$, $5P_{3/2}$ lower laser levels caused by their electron-induced deexcitation to the $4D_{3/2}$, $4D_{5/2}$ metastable states and to the $5S_{1/2}$ ground state of strontium ions.

The recombination pumping of the upper laser level and the collisional deexcitation of the lower laser levels are most efficient for a rapid and deep cooling of the electron gas during the early afterglow, which is achieved due to elastic electron collisions with light atoms and helium ions. That is why the increase in the helium pressure leads to the increase in the output energy at 430.5-nm ($6S_{1/5} \rightarrow 5P_{3/2}$) and 416.2-nm ($6S_{1/2} \rightarrow 5P_{1/2}$) lines.

Lasing in the ion spectrum of strontium is also observed at IR lines 1123, 1087, 870, and 851 nm in the recombination pumping regime at moderate helium pressures (3 – 7 Torr) as well as at 1032.7-nm and 1091.4-nm lines in the self-terminating regime at the leading edge of a current pulse. Furthermore, also possible in a strontium – krypton mixture is lasing by the $6P_{1/2,3/2} \rightarrow 6S_{1/2}$ (1245, 1201 nm) transitions arising from the charge exchange of krypton ions with strontium atoms (Fig. 1).

The active media of lasers on Sr II transitions were earlier simulated in Refs [5 – 13]. The kinetics of high-pressure active media pumped by a hard ioniser was numerically simulated in Refs [5, 9 – 12]. Active media with gas-discharge excitation were modelled in

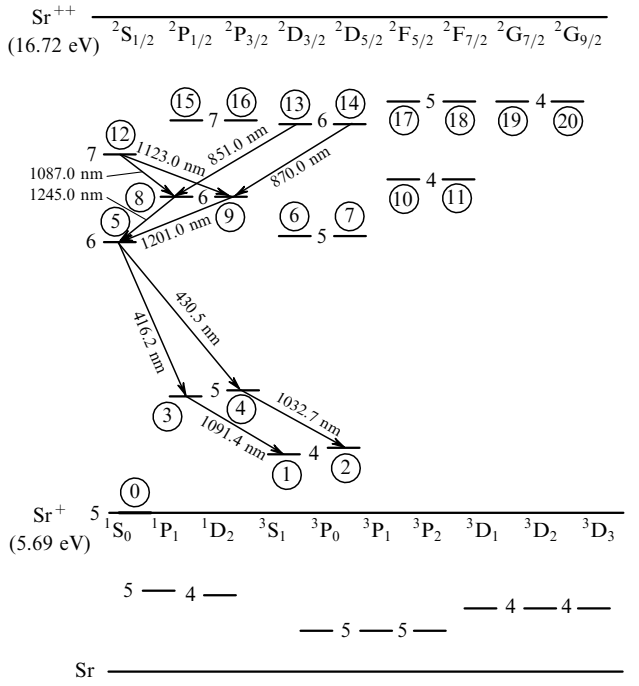

Figure 1. Energy level diagram of strontium ions; the arrows indicate the transitions that exhibit lasing, the numbering of Sr^+ ion levels accepted in the model is shown in circles.

G.D. Chebotarev, E.L. Latush, O.O. Prutsakov, A.A. Fesenko Southern Federal University, Physics Department, ul. Zorge 5, 344090 Rostov-on-Don, Russia; e-mail: latush@phys.rsu.ru

Received 1 July 2007; revision received 20 January 2008
Kvantovaya Elektronika **38** (4) 299 – 308 (2008)
Translated by E.N. Ragozin

Refs [6–8, 13]. The simplified model of Ref. [6] provided a qualitatively correct picture of the processes in the active medium. In the more detailed model [7, 8], both spatial and temporal characteristics were calculated. Reference [13] described our model of the $He-Sr^*$ laser elaborated for calculating its temporal and energy characteristics, which enabled us to perform its numerical multiparameter optimisation. In the present work, proceeding from Ref. [13] we elaborated a self-consistent mathematical model, which makes it possible to calculate the spatiotemporal evolution of the plasma parameters and of the lasing characteristics in a repetitively pulsed regime. The aim of our work is to calculate and analyse the spatiotemporal characteristics of the active medium of a $He-Sr^+$ laser. Numerical simulations will allow us to predict the optimal conditions for the excitation of active $He-Sr^+$ laser elements of different geometry, to analyse in detail the physical mechanisms that limit the improvement of output energy characteristics, and to calculate the attainable lasing parameters.

2. The mathematical model

The $He-Sr^+$ laser model comprises the description of the electrical pump circuit (the Blumlein line or a circuit with a total discharge of the storage capacitor via a thyratron), the plasma of a repetitively pulsed discharge, and the laser radiation.

Like Ref. [13], this model contains kinetic equations for the densities of long-lived plasma components: of strontium atoms N_{Sr}, metastable strontium atoms $N_{Sr^*_m}$, singly and doubly charged strontium ions N_{Sr^+} and $N_{Sr^{++}}$, helium atoms N_{He}, metastable helium atoms $N_{He^*(2^1S)}$ and $N_{He^*(2^3S)}$, helium ions N_{He^+}, metastable helium dimers $N_{He_2^*}$, molecular helium ions $N_{He_2^+}$ and complex $N_{HeSr^{++}}$ ions. The following plasmachemical processes are taken into account: elastic and inelastic electron–atom and electron–ion collisions, collisions of metastable helium atoms with ionisation, the charge exchange of ionised helium atoms and molecules with strontium atoms with the production of doubly charged strontium ions, the Penning ionisation of strontium atoms by metastable helium, three-body ion recombination, the dissociative recombination of molecular ions, atomic-to-molecular ion conversion, stepwise Penning process and stepwise charge exchange, as well as charged- and metastable-particle diffusion. The plasma is assumed to be quasi-neutral, and therefore the electron density N_e is found by summing the densities of all charged particles.

In the calculation of the level kinetics of strontium ions, 20 excited levels shown in Fig. 1 are considered. In this case, the balance equations for Sr II level populations have the form:

$$\frac{dN_i}{dt} = \sum_{j=0,\, j\neq i}^{20} (A_{j,i} + F_{j,i} + G_{j,i})N_j - \sum_{k=0,\, k\neq i}^{20} (A_{i,k} + F_{i,k} + G_{i,k})N_i - \sum_{i=1}^{20} K_{Sr_i^{+*}} N_{Sr_i^{+*}} N_e + \delta_i + W_{pi};\ i = 1, \ldots, 20, \qquad (1)$$

where $A_{i,k}$ are the optical transition probabilities (radiation trapping on the resonance transitions of Sr II is taken into account); $F_{i,k} = \langle \sigma_{i,k} v_e \rangle N_e$ are the electron excitation or deexcitation probabilities; $G_{i,k} = K_{i,k} N_{He}$ are the atomic excitation or deexcitation probabilities; $K_{Sr_i^{+*}}$ are the rate coefficients for excited state ionisation; δ_i are the terms taking into account the saturation effect on laser transitions; and W_{pi} are the partial level pumping rates.

The quantitative data on the rates of the processes listed above are presented in Ref. [13]. The main difference of the present model from that of Ref. [13] consists in that the diffusion terms of the form $6D/R^2$, where D is the diffusion coefficient and R is the radius of the laser tube, in kinetic equations for long-lived plasma components were replaced with the divergences of radial diffusion fluxes. The divergences of electron and gas thermal fluxes due to electron and gas thermal conduction were also introduced into the equations for electron and gas temperatures. As a result, this model permits calculating the spatiotemporal characteristics of the active medium.

The equation for the electron temperature T_e has the form

$$\frac{\partial}{\partial t}\left(\frac{3}{2} N_e T_e\right) = \frac{E^2\sigma}{e} - \frac{3}{2} N_e (T_e - T_g) \times \sum_{\substack{A=He,He^+,He_2^+,\\ Sr^+,Sr^{++}}} \frac{2m_e}{M_A} \nu_{eA} + \sum_{i=1}^{42} \Delta\varepsilon_i W_i - \nabla\left(\frac{3}{2} T_e \boldsymbol{\Gamma}_e\right) - \nabla \boldsymbol{\Gamma}_{eth}. \qquad (2)$$

Here, $\boldsymbol{\Gamma}_e$ and $\boldsymbol{\Gamma}_{eth}$ are the densities of electron and electron thermal diffusion fluxes in the radial direction, respectively. In Eqn (2), the first term accounts for the Joule heating of the electron gas by the electric field E (σ is the plasma conductivity), the second term for the electron cooling due to elastic collisions with heavy particles with a frequency ν_{eA}, the third one for energy liberation in the electron gas or for the energy absorption in plasmachemical processes ($\Delta\varepsilon_i$ is the energy defect and W_i are the process rates), the firth for diffusion cooling of the electron gas, and the fifth for the cooling due to electron thermal conduction.

The equation for the gas temperature T_g has the form:

$$\frac{\partial}{\partial t}\left(\frac{3}{2} N T_g\right) = \frac{3}{2} N_e (T_e - T_g) \times \sum_{\substack{A=He,He^+,He_2^+,\\ Sr^+,Sr^{++}}} \frac{2m_e}{M_A} \nu_{eA} - \nabla \boldsymbol{\Gamma}_{th}. \qquad (3)$$

Here, $\boldsymbol{\Gamma}_{th}$ is the radial thermal flux density arising from the thermal gas conduction and N is the sum of the densities of all heavy particles. In Eqn (3), the first term accounts for the gas heating due to elastic collisions with electrons and the second term for the gas cooling due to thermal conduction.

The diffusion flux densities for ions are

$$\boldsymbol{\Gamma}_i = N_i \mu_i \boldsymbol{E}_r - \frac{D_i}{T_g} \nabla (N_i T_g), \qquad (4)$$

where μ_i is the mobility of the ith ion component related to the diffusion coefficient D_i by the Einstein relation: $\mu_i = D_i / T_g$.

The diffusion electron flux density is

$$\boldsymbol{\Gamma}_e = N_e \mu_e \boldsymbol{E}_r - \frac{D_e}{T_e} \nabla (N_e T_e), \qquad (5)$$

where $\mu_e = e/(m_e \nu_{tot})$ is the electron mobility; $\boldsymbol{E}_r$ is the radial electric strength, which can be found from the condition that the diffusion electron flux is equal to the total diffusion ion flux; and ν_{tot} is the total frequency of elastic electron collisions with atoms and ions.

The diffusion flux densities for neutral particles are

$$\boldsymbol{\Gamma}_j = -\frac{D_j}{T_g} \nabla(N_j T_g), \tag{6}$$

where D_j is the diffusion coefficient of the jth neutral component.

The thermal flux density carried by the electron gas due to electron thermal conduction is

$$\boldsymbol{\Gamma}_{eth} = -\lambda_{eth} \nabla T_e \,, \tag{7}$$

where

$$\lambda_{eth} = 3.2 N_e T_e \frac{e}{m_e \nu_{tot}} \tag{8}$$

is the electron thermal conductivity coefficient [14].

The thermal flux carried by the buffer gas due to its thermal conduction is

$$\boldsymbol{\Gamma}_{th} = -\lambda_{th} \nabla T_g, \tag{9}$$

where

$$\lambda_{th} = A T_g^B \tag{10}$$

is the thermal conductivity coefficient of the buffer gas; for helium, $A = 1.55 \times 10^{21}$ cm^{-1} s^{-1} eV$^{-0.787}$; $B = 0.787$ [15].

The cylindrical symmetry condition requires that the derivatives of all plasma parameters with respect to the radial coordinate r should be equal to zero on the tube axis:

$$\frac{\partial N_i}{\partial r} = \frac{\partial T_g}{\partial r} = \frac{\partial T_e}{\partial r} = 0 \;\text{ for }\; r = 0, \tag{11}$$

where i is an arbitrary plasma component.

The boundary conditions at the wall tube for $r = R$ have the form:

$$\begin{aligned} &N_i^* = N_i^{+*} = 0, \; N_{Sr} = N_{Sr,w}, \\ &N_{He} = N_{He,w}, \; T_e = T_g = T_w, \end{aligned} \tag{12}$$

where $N_{Sr,w}$ and $N_{He,w}$ are the densities of strontium and helium atoms near the wall and T_w is the wall temperature.

The gain at the centre of the laser line is calculated from the expression [16]

$$\alpha_0 = \frac{A_{u,1}}{8\pi} \lambda^2 \left(N_u - \frac{g_u}{g_l} N_l \right) g(\nu_0), \tag{13}$$

where $A_{u,1}$ and λ are the probability and wavelength of the laser transition; N_l and N_u are the populations of the lower and upper working levels; and g_l and g_u are the statistical weights of these levels. The form factor $g(\nu_0)$ at the centre of a line with the Voigt profile is approximated by the function [17]:

$$g(\nu_0) = \frac{2\sqrt{\ln 2}}{\sqrt{\pi}\,\Delta\nu_G \left[\sqrt{\pi}\, a/2 + (1 + \pi a^2/4)^{1/2}\right]} \times \frac{1}{1 + 0.1667 a^{0.845} \exp(-1.167 a)}. \tag{14}$$

Here, $a = \sqrt{\ln 2}\,\Delta\nu_L / \Delta\nu_G$; $\Delta\nu_L$ is the width of the Lorentzian profile due to collisional and Stark broadening; and $\Delta\nu_G$ is the width of the Gaussian profile arising from the Doppler effect.

The following equations are added to the overall set of equations to calculate the intensity of intracavity laser field [18]:

$$\frac{dI_{c(416.2)}}{dt} = c I_{c(416.2)} \left(\alpha_{0(416.2)} \frac{l_a}{l_c} - \eta_1 - \eta_2 \right) + \frac{1}{16} \frac{c^2 h}{\lambda_{5,3}} A_{5,3} N_{Sr^{+*}} \frac{d^2}{l_a^2}, \tag{15}$$

$$\frac{dI_{c(430.5)}}{dt} = c I_{c(430.5)} \left(\alpha_{0(430.5)} \frac{l_a}{l_c} - \eta_1 - \eta_2 \right) + \frac{1}{16} \frac{c^2 h}{\lambda_{5,4}} A_{5,4} N_{Sr^{+*}} \frac{d^2}{l_a^2}, \tag{16}$$

where $\alpha_{0(416.2)}$ and $\alpha_{0(430.5)}$, $I_{c(416.2)}$ and $I_{c(430.5)}$ are the gain and intracavity laser field intensities for the 416.2- and 430.5-nm lines of Sr II ions, respectively; $\eta_1 = (2l_c)^{-1} \ln (R_1 R_2)^{-1}$ and η_2 are the coefficients of useful and adverse losses in the resonator, respectively; l_c and l_a are the lengths of the resonator and the active medium; d is the diameter of the discharge tube; $N_{Sr^{+*}}$ is the population density of the upper laser level; and R_1 and R_2 the reflectivities of resonator mirror. The last term in Eqns (15) and (16) describes the spontaneous seed for laser radiation.

The spontaneous emission intensities of strontium ion lines were calculated taking into account amplification effects (or self-absorption) from the expression [19, 20]

$$I_{ASE} = \frac{1}{4\pi} N_u A_{u,1} h\nu l_a S'(\alpha_0 l_a), \tag{17}$$

where

$$S'(\alpha_0 l_a) = \frac{1}{\pi \alpha_0 l_a} \int_{-\infty}^{\infty} \left[\exp\left(\alpha_0 l_a \frac{1}{\omega^2 + 1} \right) - 1 \right] d\omega \tag{18}$$

is the Ladenburg–Reiche function [19] (amplification is taken into account for $\alpha_0 > 0$ and self-absorption for $\alpha_0 < 0$);

$$\omega = \frac{2(\nu - \nu_0)}{\Delta\nu_L}. \tag{19}$$

To simplify the calculations here we restricted ourselves to the consideration of the Lorentzian Sr II line profile, which makes the dominant contribution to the resultant Voigt profile.

The output laser radiation intensity I is calculated in terms of the intracavity laser field intensity I_c and the useful loss coefficient η_1 [18]:

$$I = \eta_1 I_c l_c. \tag{20}$$

The pulsed lasing power P may be found by integrating expression (20) over the cross section of the laser tube:

$$P = 2\pi \int_0^R I(r) r \, \mathrm{d}r. \tag{21}$$

The laser pulse energy $\mathscr{E}$ is found by integrating the lasing power with respect to the time:

$$\mathscr{E} = \int_0^\infty P \mathrm{d}t. \tag{22}$$

The average output power in the repetitively pulsed regime is calculated proceeding from the laser pulse energy $\mathscr{E}$ and the pulse repetition rate f:

$$P_{\mathrm{av}} = \mathscr{E} f. \tag{23}$$

The initial data in the calculations are the length l_a of the active medium and the internal diameter d of the laser tube, the cavity length l_c, the reflectivities R_1 and R_2 of the mirrors, the temperature T_w of the inner tube wall, the radially uniform initial pressure p^0_{He} of the buffer helium gas, the density $N_{\mathrm{Sr,w}}$ of strontium atoms near the wall, and the discharge circuit parameters.

In the self-heating regime, the density $N_{\mathrm{Sr,w}}$ is calculated proceeding from the value of T_w using a formula which approximates the reference data on the saturated strontium vapour pressure [21]:

$$N_{\mathrm{Sr,w}} = 6.247 \times 10^{12} \, \frac{10^{(10.53 - 0.7239/T_w)}}{T_w}, \tag{24}$$

where T_w is taken in electron-volts.

The initial density distributions of strontium atoms N^0_{Sr} and helium N^0_{He} are assumed to be uniform over the tube radius:

$$N^0_{\mathrm{Sr}} = N_{\mathrm{Sr,w}}, \tag{25}$$

$$N^0_{\mathrm{He}} = 8.324 \times 10^{14} \, \frac{p^0_{\mathrm{He}}}{T_w}. \tag{26}$$

Equation (26) is the equation of state for helium, where p^0_{He} is taken in Torrs and T_w – in electron-volts. The initial gas temperature is also assumed to be radially uniform and equal to T_w. The initial densities of the remaining particles, the seed values are taken to be small.

In the simulations the initial conditions are improved after calculating the first plasma excitation–relaxation cycle. The new set of initial conditions is used in the calculation of the next excitation–relaxation cycle, etc. The calculations are repeated until a pulse-to-pulse reproducibility of plasma parameters of better than $\sim 1\,\%$ is reached, which corresponds to the steady-state regime.

3. Spatiotemporal characteristics

Consider the establishment of the repetitively pulsed regime of the $He-Sr^+$ laser employing the results of simulations carried out for the conditions of Ref. [22].

Figures 2a and 2b show the peak current i_{peak} and the peak lasing intensity I_{peak} in the afterglow on the 430.5-nm line of Sr II ions for the first 60 pulses. One can see that the current is relatively low (~ 250 A) during the first pulse due to the high resistance of the active medium prior to the first pulse. Subsequently, from pulse to pulse the prepulse electron density increases (Fig. 2d), the plasma conductivity rises, and the peak current increases several-fold (Fig. 2a). In this case, the pumping rate increases and hence the peak intensity of lasing (Fig. 2b). Due to heat accumulation, the

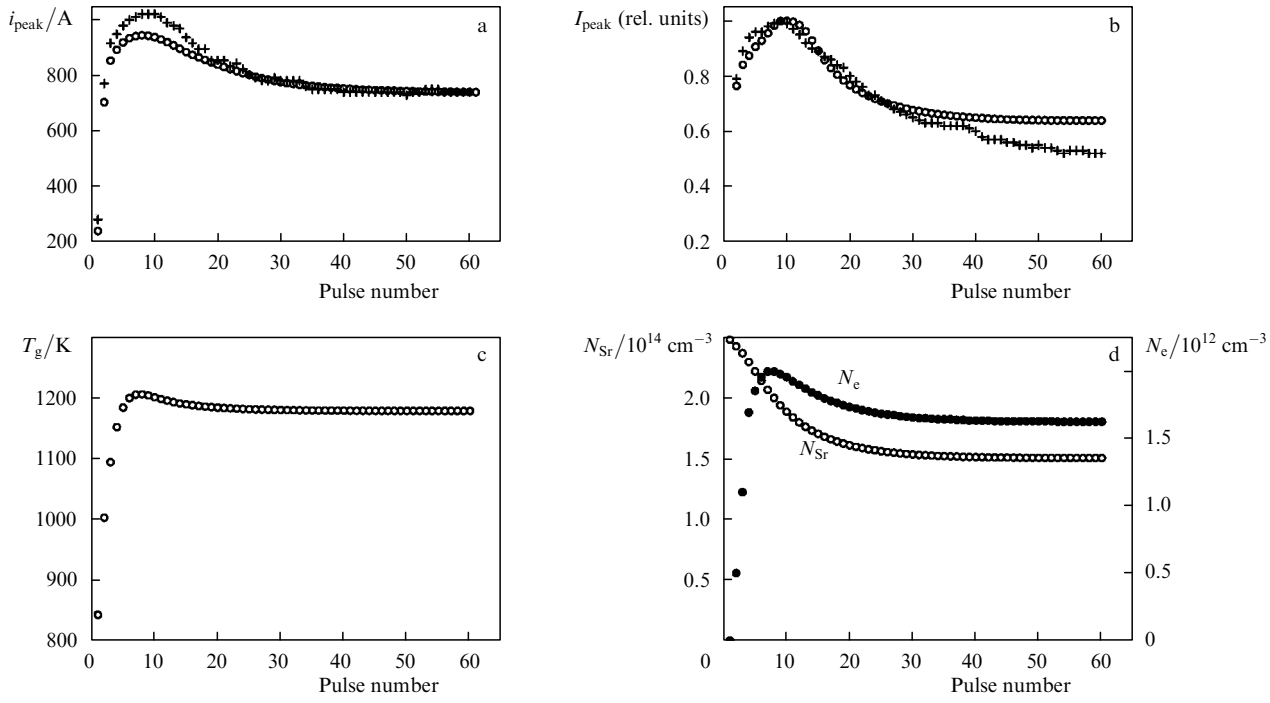

Figure 2. Peak current (a) and peak lasing power for the 430.5-nm line of Sr II ions (b) calculated for the first 60 pulses (circles) and experimentally observed [22] (crosses), as well as calculated gas temperature (c) and prepulse densities of strontium atoms and electrons (d) on the tube axis ($l_a = 40$ cm, $d = 2.5$ cm, $p^0_{\mathrm{He}} = 200$ Torr, $N^0_{\mathrm{Sr}} = 2.5 \times 10^{14}$ cm^{-3}, $f = 1.16$ kHz).

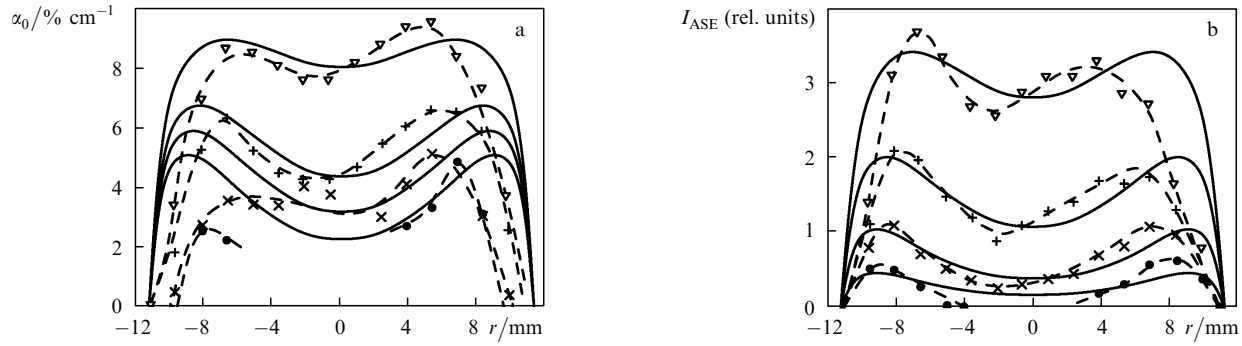

Figure 3. Calculated (solid curves) and measured [22] (dashed curves) radial profiles of the unsaturated gain (a) and the amplified spontaneous emission intensity of the 430.5-nm Sr II line (b) at different instants of time relative to the instant of cessation of the current pulse [50 (▽), 100 (+), 200 (×), and 300 ns (●)] ($l_a = 40$ cm, $d = 2.5$ cm, $p^0_{He} = 200$ Torr, $N^0_{Sr} = 2.5 \times 10^{14}$ cm^{-3}, $f = 0.7$ kHz).

gas temperature on the tube axis builds up (Fig. 2c), which leads to a lowering of the prepulse density N_{Sr} of strontium atoms (Fig. 2d) caused by the thermal diffusion and radial cataphoresis of metal vapour. Such is the case up to about the 10th pulse.

The lowering of the prepulse density N_{Sr} on the axis is responsible for a density lowering of doubly charged strontium ions produced in the ionisation during the current pulse. This results in a decrease of recombination pumping rate and a fall of the output intensity after approximately the 10th pulse (Fig. 2b) as well as in a lowering of Sr^+ and Sr^{++} ion densities in the afterglow. Accordingly there lowers the prepulse density N_e (Fig. 2d), which is primarily defined by singly charged strontium ions having a lower recombination rate in comparison with doubly charged ions. Furthermore, the peak current decreases (Fig. 2a), because the paraxial regions of the active medium show a lowering of the plasma conductivity, which is largely determined by the density of strontium atoms and decreases as this density becomes lower. This is due to the fact that the atoms and singly charged ions of strontium are first to become ionised, because the first (5.69 eV) and second (11.03 eV) ionisation potentials of strontium are considerably lower than the first ionisation potential of helium (24.59 eV). The insignificant lowering of the on-axis gas temperature (Fig. 2c) occurring after approximately the 10th pulse is caused by the transformation of the radial profile of heat release. As suggested by Fig. 2, the steady-state repetitively pulsed regime is formed in 40 – 50 pulses.

Figure 3 shows the calculated and measured [22] radial profiles of the unsaturated gain coefficient α_0 and the amplified spontaneous emission intensity I_{ASE} of the 430.5-nm Sr II ion line in the steady-state regime at different instants of time. The axial gain and intensity minima arise from the fact that the density of $N_{Sr^{++}}$ and hence the recombination pumping rate show a minimum on the axis due to the on-axis lowering of the prepulse N_{Sr} density (Fig. 2d).

Let us analyse the spatiotemporal dependences of the plasma parameters and the lasing characteristics of the $He - Sr^+$ laser in the steady-state repetitively pulsed regime under the conditions of Refs [23, 24].

Figure 4 shows the calculated and experimentally observed [23] pulses of the current and the amplified spontaneous emission for the 430.5-nm line. The calculated prepulse radial distributions of the strontium atomic and ion densities are depicted in Fig. 5a, the density of helium

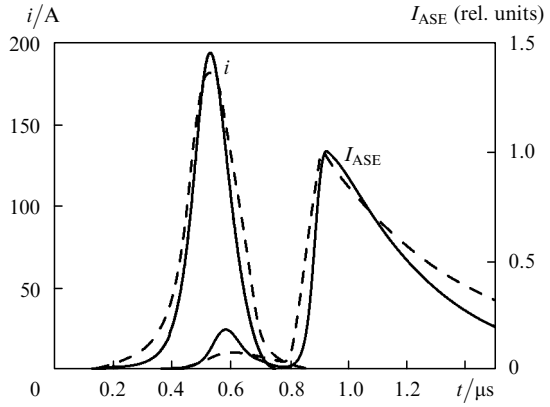

Figure 4. Pulses of discharge current and amplified spontaneous emission for the 430.5-nm line of Sr II ions calculated (solid curves) and measured in Ref. [23] (dashed curves) ($l_a = 66$ cm, $d = 1.27$ cm, $p^0_{He} = 112.5$ Torr, $N^0_{Sr} = 2.75 \times 10^{14}$ cm^{-3}, $f = 3.77$ kHz).

atoms, the gas and electron temperatures are shown in Fig. 5b. Also shown in Fig. 5a are the experimental prepulse radial profiles of the densities N_{Sr} and N_{Sr^+}.

Figures 5c, 5d, and 5e show the spatiotemporal evolution of the densities of the atoms, ions, and doubly charged ions of strontium, respectively. One can see that during the excitation pulse the atoms of strontium ionise and pass into doubly charged ions almost completely, with a substantial amount of singly charged ions present only near the wall. In the afterglow, the doubly charged ions recombine to singly charged ions rather rapidly, this recombination proceeding more intensely at the centre than at the periphery, because the electron density is highest at the centre (Fig. 5f).

Figure 5g depicts the spatiotemporal dependence of the unsaturated gain and Fig. 5h shows the 430.5-nm line lasing intensity. One can see that under these conditions the population inversion and the lasing intensity are maximal at the centre. However, as the Sr^{++} ions recombine, the lasing becomes weaker in the paraxial region and 'shifts' to the periphery (Fig. 5g), where the doubly charged metal ions are still relatively abundant (Fig. 5e).

Figures 6 and 7 give the data calculated for the conditions of Ref. [24]. Figure 6 depicts the calculated and experimentally measured pulses of current and lasing for the 430.5-nm line. A short time delay between the experimental and calculated pulses is caused by the delay of recombination pump 'engagement' due to electron gas

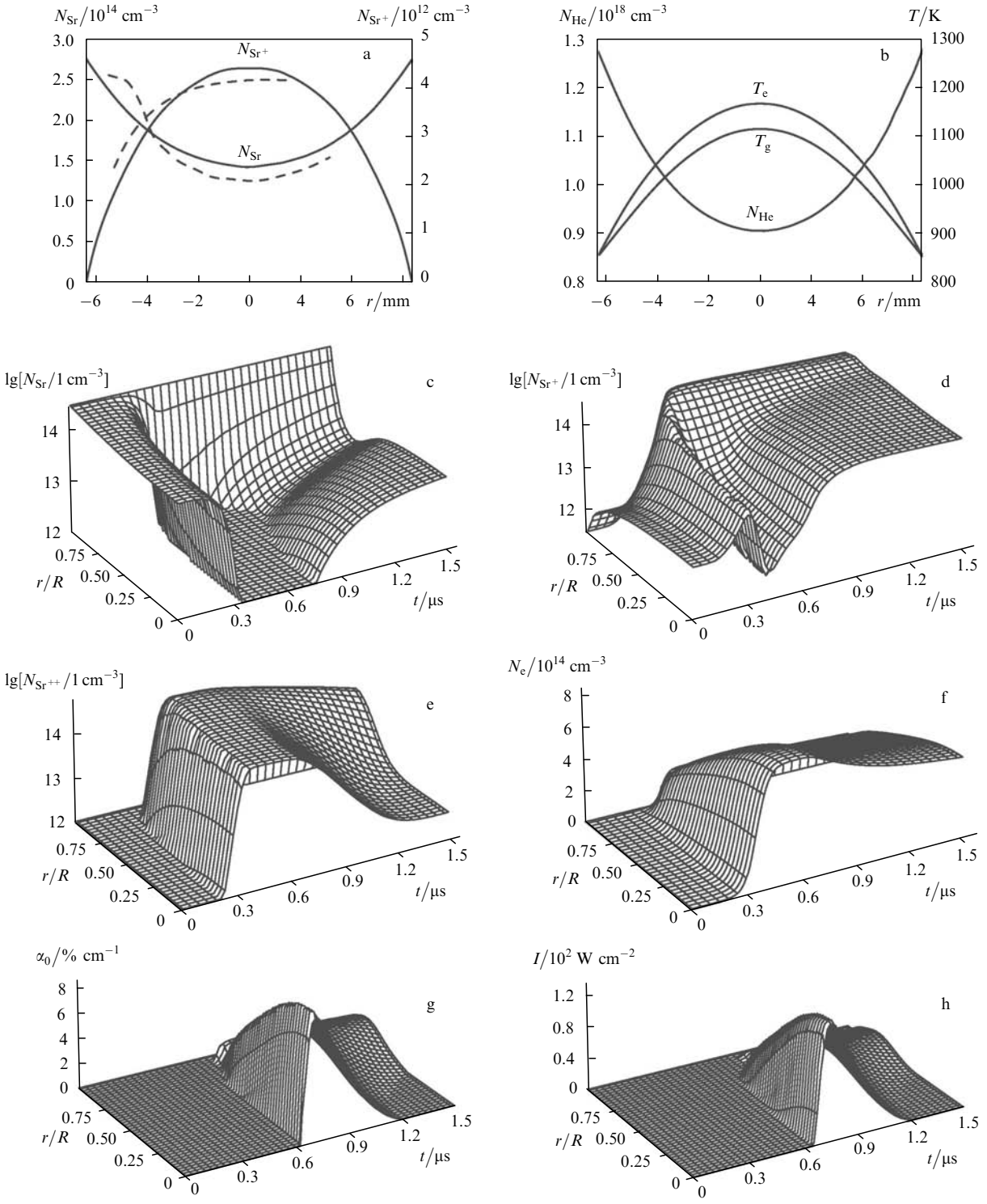

Figure 5. Calculated radial prepulse profiles of the strontium atomic and ion densities (a), the atomic helium density, the gas and electron temperatures (b), spatiotemporal dependences of the densities of strontium atoms (c), singly charged strontium ions (d), doubly charged strontium ions (e), and electrons (f), as well as of the unsaturated gain (g) and the intensity of 430.5-nm Sr II ion line lasing (h); dashed curves – experiment of Ref. [23] ($l_a = 66$ cm, $d = 1.27$ cm, $p^0_{He} = 112.5$ Torr, $N^0_{Sr} = 2.75 \times 10^{14}$ cm^{-3}, $f = 3.77$ kHz).

heating, which is caused by the step at the trailing edge of the experimentally observed current pulse arising from the insufficient matching of the discharge tube with the electrical pump circuit. This temporal shift was taken into account in Figs 7a and 7b, which show the radial profiles of the electron density at different instants of time relative to the current peak and the profile of the electron temperature in the afterglow at the instant of peak lasing.

The spatiotemporal dependences of the electron and gas temperatures, the densities of strontium atoms, singly and doubly charged ions, as well as the intensities of lasing at the 430.5-nm line are given in Figs 7c – 7h. One can see that the gas temperature varies only slightly during the course of the pulse in the steady-state regime (Fig. 7d). It is radially nonuniform, which is responsible for a radial cataphoresis along with a nonuniform prepulse radial distribution of

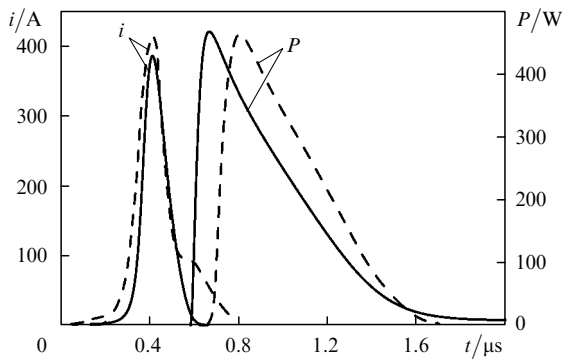

Figure 6. Pulses of the discharge current and 430.5-nm Sr II ion line lasing calculated (solid curves) and measured in Ref. [24] (dashed lines) ($l_a = 70$ cm, $d = 1.55$ cm, $p^0_{He} = 250$ Torr, $N^0_{Sr} = 4.2 \times 10^{14}$ cm^{-3}, $f = 6$ kHz).

metal atoms with a dip on the axis (Fig. 7e). At the end of the excitation pulse, the radial $N_{Sr^{++}}$ density profile (Fig. 7g) practically replicates (with the exception of thin regions at the walls) the prepulse profile of the atomic strontium density (Fig. 7e), which experience an almost complete double ionisation during the excitation pulse. The axial dip in the $N_{Sr^{++}}$ distribution leads to the minimum of lasing intensity on the tube axis (Fig. 7h). A radial lasing intensity profile with a small dip on the axis is typical for a $He - Sr^+$ laser operating at a rather high helium pressure [22, 25].

When the $He-Sr^+$ laser evolves to the steady-state thermal regime, the physically interesting and practically important effect of decontraction of the repetitively pulsed discharge is observed: in a 'cool' laser tube void of strontium vapour, the discharge in helium is contracted and exists in

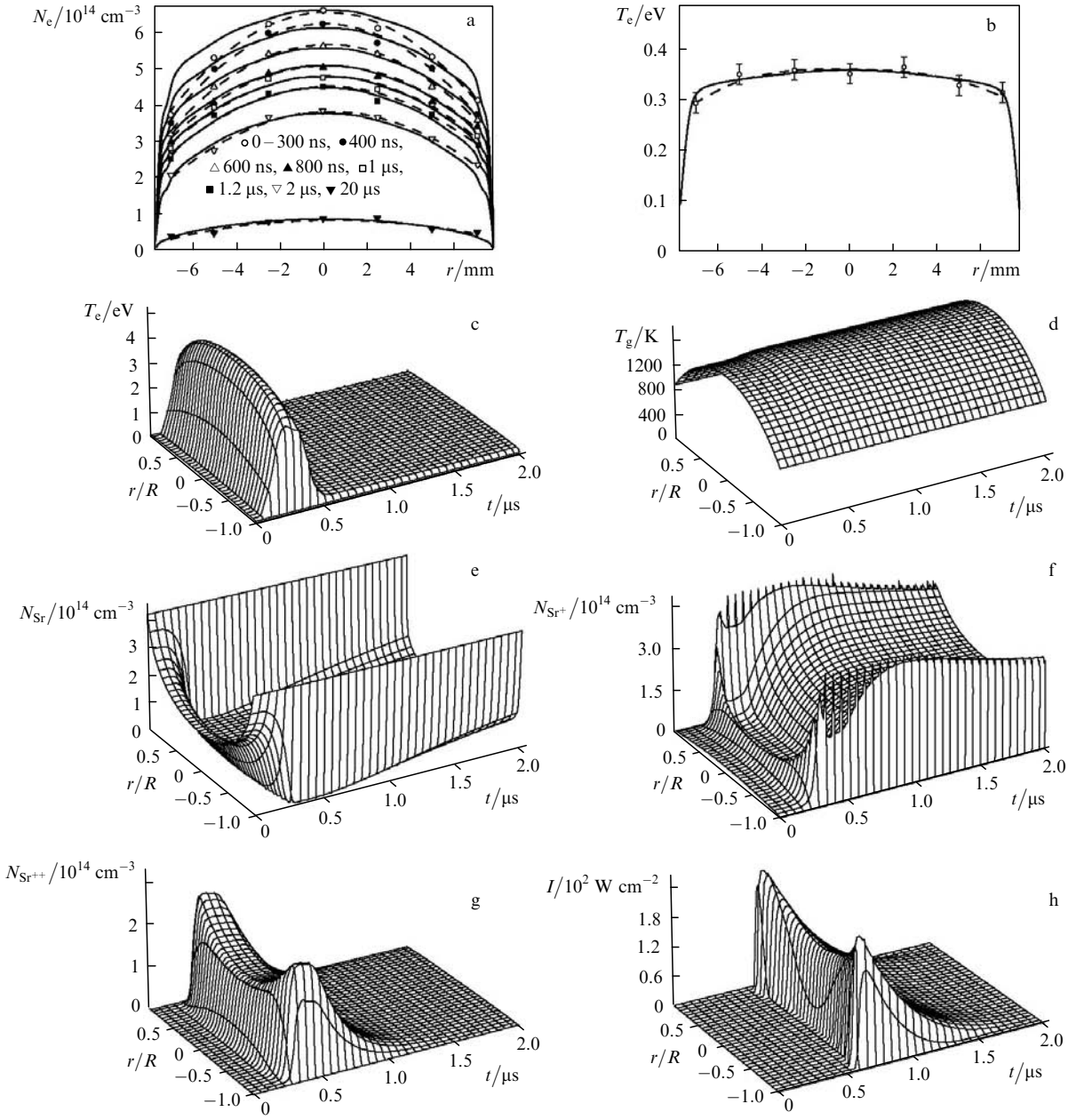

Figure 7. Calculated radial profiles of the electron density at different instants of time relative to the moment at which the current passes through its maximum (a) and of the electron temperature at instant of maximum lasing (b), as well as the spatiotemporal dependences of the electron temperature (c), the gas temperature (d), the densities of strontium atoms (e), singly (f) and doubly (g) charged strontium ions, and the intensity of lasing on the 430.5-nm Sr II ion line (h); dashed curves – experiments of Ref. [24] ($l_a = 70$ cm, $d = 1.55$ cm, $p^0_{He} = 250$ Torr, $N^0_{Sr} = 4.2 \times 10^{14}$ cm^{-3}, $f = 6$ kHz).

the form of a thin column; on tube heating and arrival of strontium vapour in the discharge, there occurs discharge decontraction – it fills the entire tube section. In this case, the plasma becomes virtually uniform to provide high lasing energy characteristics [25–30]. Let us analyse the contraction and decontraction of the repetitively pulsed discharge.

Figure 8 shows the radial distributions of plasma parameters calculated for different sequential excitation pulses (conditions as in Ref. [24]). The seed uniform distributions of all plasma parameters were taken as the initial conditions for the first pulse. Modelled up to the 60th pulse was a pure helium discharge, and after that a discharge in a helium–strontium mixture.

One can see that there occurs helium discharge contraction after approximately 40 pulses. This number of pulses corresponds to the steady-state settling time (~ 6 ms). Figure 8e suggests that initially, when the gas just begins to warm up (Fig. 8c), the helium density does not manage to immediately respond to a change in temperature, because to do this requires time $\tau_{\text{diff}} = R^2(6D_{\text{He}})^{-1} \approx 4$ ms. As a result, the helium pressure builds up (Fig. 8f), since $p_{\text{He}} \propto N_{\text{He}}T_{\text{g}}$. The gas temperature settling time is defined by the quantity $\tau_{\text{th}} = R^2/6\chi \approx 2$ ms, where χ is the thermal diffusivity of helium. Since T_{g} and N_{He} are related, the steady-state settling time will be equal to about the sum of the times $\tau_{\text{diff}} + \tau_{\text{th}} \approx 6$ ms. In the steady-state regime, the helium pressure is constant over the radius (Fig. 8f) and the prepulse radial profile of the density N_{He} (Fig. 8e) turns out to be the 'reverse' of the T_{e} profile (Fig. 8c).

The decrease of the axial helium density due to the gas heating leads to a growth in T_{e} on the axis (Fig. 8b), because $T_{\text{e}} \propto E/N_{\text{He}}$, where E is the field intensity. Due to the high ionisation and excitation potentials of helium, its ionisation rate is highly sensitive to variations in T_{e} along the tube radius and turns out to be highest on the axis. As a result, the density N_{e} (Fig. 8a) and the plasma conductivity σ (Fig. 8d) rise sharply on the axis, i.e. there occurs discharge contraction.

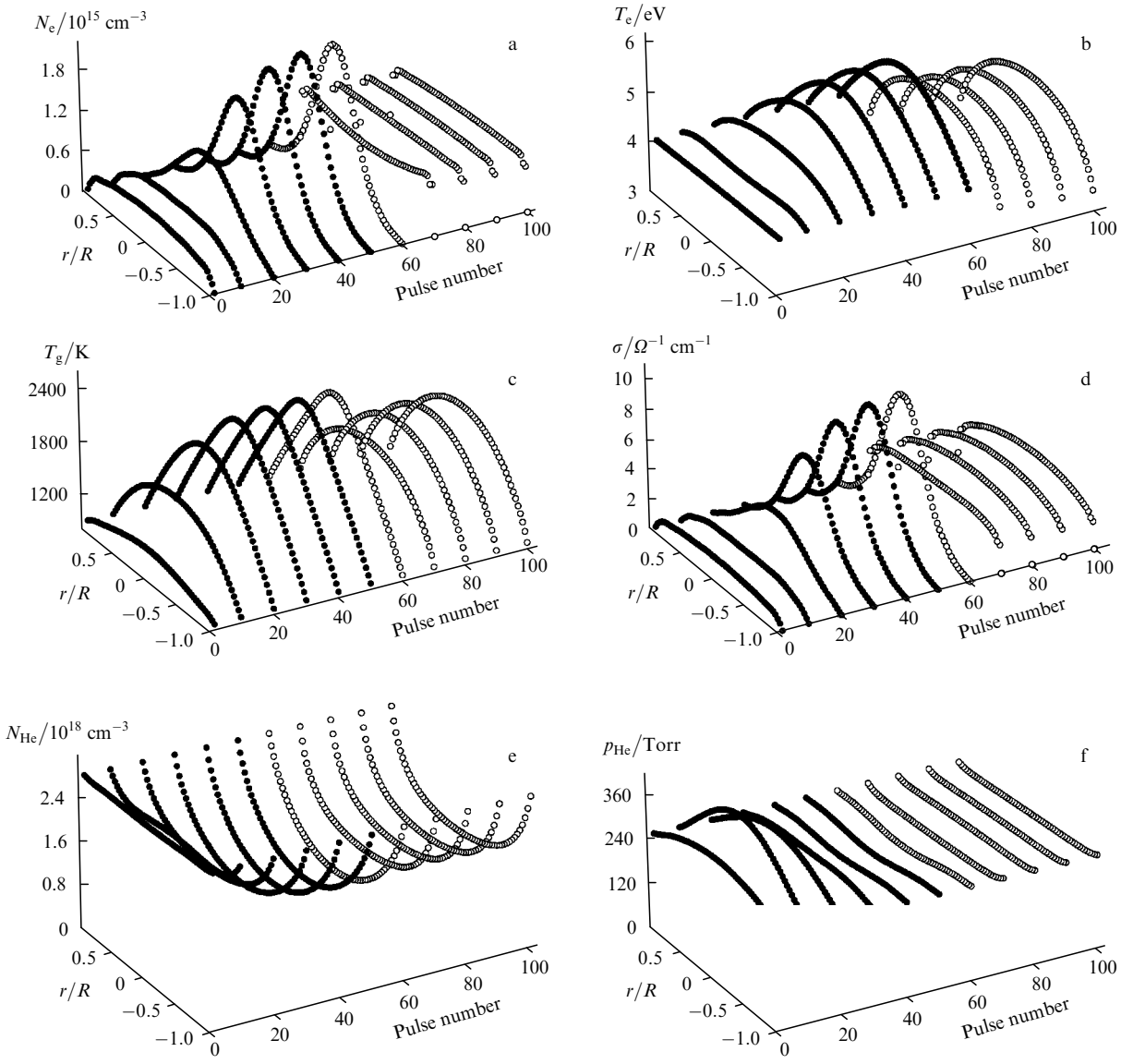

Figure 8. Radial profiles of the electron density (a), electron temperature (b), gas temperature (c), plasma conductivity (d) and prepulse radial profiles of the helium density (e) and pressure (f) calculated for different sequential excitation pulses. Modelled up to the 60th pulse was a pure helium discharge, and after that a discharge in a helium–strontium mixture for $N_{\text{Sr}}^0 = 4 \times 10^{14}$ cm^{-3} ($l_{\text{a}} = 70$ cm, $d = 1.55$ cm, $p_{\text{He}}^0 = 190$ Torr, $f = 6$ kHz).

As is evident from Fig. 8, the energy of a single excitation pulse is insufficient to substantially heat the gas, and therefore the discharge does not experience appreciable contraction in a single pulse. However, in a repetitively pulsed regime, when $1/f \ll \tau_{diff} + \tau_{th}$, the heat accumulates from pulse to pulse until the radial distribution of T_g evolves to the stationary state with a strongly pronounced maximum on the axis (Fig. 8c). The thermal plasma nonuniformity which is formed under the pulse sequence eventually leads to discharge contraction (Figs 8a and 8d).

In our simulations, strontium atoms were introduced into the plasma prior to the 60th pulse. Referring to Fig. 8, the decontraction proceeds rather fast: by the 70th pulse the discharge is completely decontracted. In this case, there occurs an on-axis lowering of the gas and electron temperatures, the electron density, and the plasma conductivity. The radial distributions of N_e and σ become almost flat.

Also, the discharge decontraction is well illustrated in Fig. 9, which depicts the stationary radial distributions of the plasma parameters by the end of a current pulse, when the density of N_e is highest, calculated for different additions of strontium. Figure 9a also gives the experimentally obtained radial N_e density profile in pure helium [24]. One can see that the addition of strontium exerts a significant effect when $N_{Sr}^0 \geqslant 5 \times 10^{13}$ cm^{-3}. For $N_{Sr}^0 = 4 \times 10^{14}$ cm^{-3} the plasma becomes virtually uniform (Figs 9a and 9d).

Our analysis (see also Ref. [30]) suggests that the discharge decontraction on the introduction of strontium

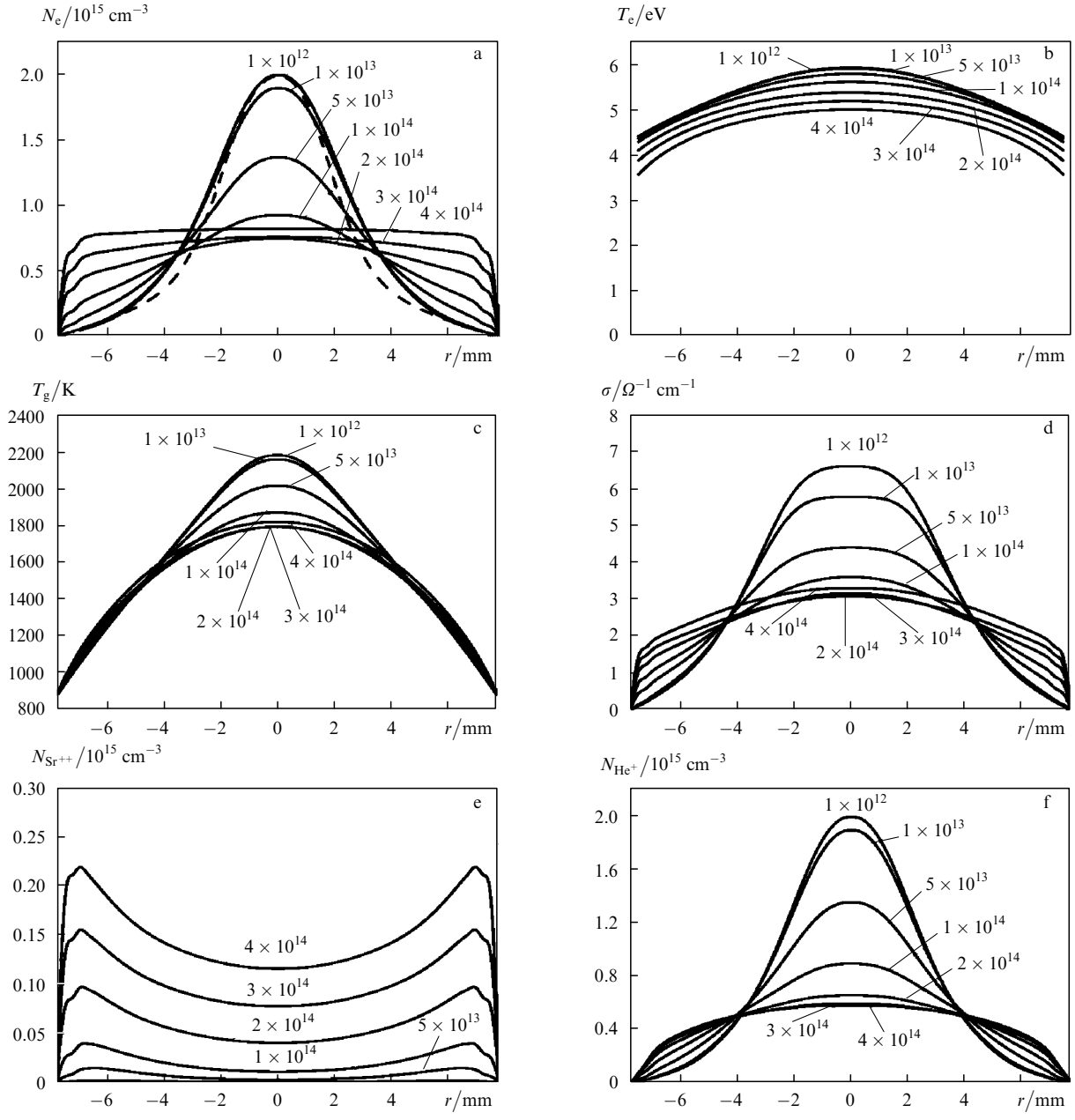

Figure 9. Calculated radial profiles of the electron density (a), electron temperature (b), gas temperature (c), plasma conductivity (d), densities of doubly charged strontium ions (e) and helium ions (f); the values of N_{Sr}^0 are indicated by the curves, the dashed curve represents the experiment of Ref. [24] in pure helium ($l_a = 70$ cm, $d = 1.55$ cm, $p_{He}^0 = 190$ Torr, $f = 6$ kHz).

atoms is primarily caused by their low ionisation potential. In this case, there occurs an almost complete double ionisation of strontium virtually throughout the entire lateral discharge section (Fig. 9e). This is responsible for a growth in N_e and plasma conductivity in the near-wall region (Figs 9a and 9d) and hence in a growth of the heat release at the wall and, under the conditions of constant energy input into the discharge, the corresponding lowering of the axial heat release. The smoothing of the radial heat release profile occurring in this way in turn leads to a substantial lowering of the gas temperature in the axial discharge region and its moderate increase near the wall (Fig. 9c). These changes of the gas temperature profile as well as the growth of electron-gas energy loss for the ionisation of strontium are responsible for some lowering of the level of electron temperature and for a decrease in its radial drop across the tube (Fig. 9b). As a result, due to the sharp dependence of the helium ionisation rate on T_e there occurs a spatial stabilisation of the ionisation of the buffer gas (Fig. 9f), whose ions make a substantial contribution to the resultant radial profile of the density N_e along with singly and doubly charged metal ions. Eventually, as N_{Sr}^0 increases, N_e and σ flatten over the tube radius (Figs 9a and 9d).

The decontraction effect is of considerable importance for the physics of metal vapour lasers as well as for gas discharge physics as a whole, because it automatically ensures rather high spatial plasma uniformity at high pressures.

Calculations involving variation of the mixture component densities show that retaining the spatial plasma uniformity at higher helium pressures requires raising the density of strontium. The ratios between the mixture components required in this case turn out to be close to the ratios that afford the highest recombination pumping rate and the optimal energy characteristics of lasing. This favours a rapid improvement of the pulse energy characteristics of the $He-Sr^+$ laser with increasing pressure.

4. Conclusions

By using a self-consistent mathematical model of a recombination $He-Sr^+$ laser, we calculated and analysed the characteristics of the active medium: the establishment of the repetitively pulsed regime was investigated, the spatiotemporal characteristics of plasma and lasing in the steady-state regime were comprehensively analysed, and a study was made of the contraction of a repetitively pulsed discharge in helium and of the discharge decontraction on introduction of strontium vapour, which is fundamentally important for metal vapour lasers and which automatically ensures a relatively high spatial plasma uniformity at high pressures. Numerical simulations may be a useful tool in the investigation of the active medium kinetics of a $He-Sr^+$ laser as well as enables predicting the optimal excitation conditions and calculating the limiting attainable lasing characteristics.

References

1. Ivanov I.G., Latush E.L., Sem M.F. *Ionnye lazery na parakh metallov* (Metal Vapour Ion Lasers) (Moscow: Energoatomizdat, 1990).
2. Ivanov I.G., Latush E.L., Sem M.F. *Metal Vapour Ion Lasers: Kinetic Processes and Gas Discharges* (Chichester, New York: John Willey & Sons, 1996).
3. Little C.E. *Metal Vapour Lasers: Physics, Engineering and Applications* (Chichester, New York: John Willey & Sons, 1999).
4. *Entsiklopediya nizkotemperaturnoi plazmy. Tom XI-4, Gazovye i plazmennye lazery* (Encyclopedia of Low Temperature Plasma. Vol. XI-4, Gas and Plasma Lasers) (Moscow: Fizmatgiz, 2005).
5. Babenko S.M., Yakovlenko S.I. Preprint IAE No. 3192 (Moscow, 1979).
6. Bukshpun L.M., Latush E.L. VINITI deposit No. 62-98-B87 (Moscow, 1987).
7. Carman R.J. *IEEE J. Quantum Electron.*, **26**, 1588 (1990).
8. Carman R.J. *J. Phys. D.*, **24**, 1803 (1991).
9. Karelin A.V., Yakovlenko S.I. *Kvantovaya Electron.*, **20**, 631 (1993) [*Quantum Electron.*, **23**, 545 (1993)].
10. Karelin A.V., Yakovlenko S.I. *Sov. J. Laser Research*, **15**, 1 (1994).
11. Karelin A.V., Shirokov R.V. *Kvantovaya Electron.*, **24**, 419 (1997) [*Quantum Electron.*, **27**, 407 (1997)].
12. Karelin A.V., Tarasenko V.F., Yakovlenko S.I. *Laser Phys.*, **10**, 827 (2000).
13. Chebotarev G.D., Prutsakov O.O., Latush E.L. *Proc. SPIE Int. Soc. Opt. Eng.*, **5483**, 83 (2004).
14. Cheng C., Sun W. *Opt. Commun.*, **144**, 109 (1997).
15. Batenin V.M., Buchanov V.V., Kazaryan M.A., Klimovskii I.I., Molodykh E.I. *Lazery na samoogranichennykh perekhodakh atomov metallov* (Lasers on Self-Terminating Transitions of Metal Atoms) (Moscow: Nauchnaya Kniga, 1998).
16. Zvelto O. *Principles of Lasers* (New York: Plenum Press, 1982).
17. Chebotarev G.D., Latush E.L. *Kvantovaya Electron.*, **20**, 99 (1993) [*Quantum Electron.*, **23**, 85 (1993)].
18. Tarasov L.V. *Fizika protsessov v generatorakh kogerentnogo opticheskogo izlucheniya* (The Physics of Processes in the Generators of Coherent Optical Radiation) (Moscow: Radio i Svyaz', 1981).
19. Frish S.E. (Ed.) *Spektroskopiya gazorazryadnoi plazmy* (Spectroscopy of a Gas-Discharge Plasma) (Leningrad: Nauka, 1970).
20. Chebotarev G.D., Latush E.L., Sem M.F. *Opt. Spektrosk.*, **81**, 688 (1996).
21. Grigor'ev I.S., Meilikhov E.Z. (Eds) *Fizicheskie velichiny* (Handbook of Physical Quantities) (Moscow: Energoatomizdat, 1991).
22. Little C.E., Piper J.A. *IEEE J. Quantum Electron.*, **26**, 903 (1990).
23. Kunnemeyer R., McLucas C.W., Brown D.J.W., McIntosh A.I. *IEEE J. Quantum Electron.*, **23**, 2028 (1987).
24. Loveland D.G., Webb C.E. *J. Phys. D: Appl. Phys.*, **25**, 597 (1992).
25. Bokhan P.A., Zakrevskii D.E. *Zh. Tekh. Fiz.*, **67**, 25 (1997).
26. Bukshpun L.M., Latush E.L., Sem M.F. *Kvantovaya Electron.*, **15**, 1762 (1988) [*Sov. J. Quantum Electron.*, **18**, 1098 (1988)].
27. Klimkin V.M. Preprint IOA SO RAN No. 1 (Tomsk, 1999).
28. Bokhan P.A., Zakrevskii D.E. *Pis'ma Zh. Eksp. Teor. Fiz.*, **62**, 26 (1995).
29. Klimkin V. *Proc. SPIE Int. Soc. Opt. Eng.*, **4747**, 164 (2002).
30. Chebotarev G.D., Prutsakov O.O., Latush E.L. *Opt. Atmos. Okean.*, **19**, 113 (2006).